

# Using Sky-pointing fish-eye camera and LiDAR to aid GNSS single-point positioning in urban canyons

Xiwei Bai<sup>1</sup>, Weisong Wen<sup>2</sup>, Li-Ta Hsu<sup>1</sup>

<sup>1</sup>Interdisciplinary Division of Aeronautical and Aviation Engineering, The Hong Kong Polytechnic University, Kowloon 518000, Hong Kong

<sup>2</sup>Department of Mechanical Engineering, The Hong Kong Polytechnic University, Kowloon, Hong Kong

E-mail: 17902061r@connect.polyu.hk

**Abstract:** Robust and globally-referenced positioning is indispensable for autonomous driving vehicles. Global navigation satellite system (GNSS) is still an irreplaceable sensor. Satisfactory accuracy (about 1 m) can be obtained in sparse areas. However, the GNSS positioning error can be up to 100 m in dense urban areas due to the multipath effects and non-line-of-sight (NLOS) receptions caused by reflection and blockage from buildings. NLOS is currently the dominant factor degrading the performance of GNSS positioning. Recently, the camera has been employed to detect the NLOS and then to exclude the NLOS measurements from GNSS calculation. The exclusion of NLOS measurements can cause severe distortion of satellite distribution, due to the excessive NLOS receptions in deep urban canyons. Correcting the NLOS receptions with the aid of 3D light detection and ranging after detection of NLOS receptions using a fish-eye camera was proposed in this study. Finally, the GNSS positioning was improved by using the healthy and corrected NLOS pseudo-range measurements. The proposed method is evaluated through real road tests in typical highly urbanised canyons of Hong Kong. The evaluation results show that the proposed method can effectively improve the positioning performance.

## 1 Introduction

Insufficient positioning accuracy [1] in urban canyon areas is still one of the key problems that postpone the arrival of the large population of autonomous systems [2]. Light detection and ranging (LiDAR), camera, and inertial navigation system (INS) [3] are usually integrated with global navigation satellite system (GNSS) positioning [4–7] to obtain robust positioning. In the integration, the GNSS receiver is the one that can continually provide absolute positioning. It can provide satisfactory performance if the receiver receives enough directly transmitted signals. However, the GNSS transmission may be reflected, diffracted, or blocked by surrounding buildings and moving objects in a dense urban canyon, such as Hong Kong, which can cause additional signal transmission delay. Thus, it introduces additional pseudo-range errors due to both multipath effect and non-light-of-sight (NLOS) reception. As a result, the positioning error can be up to 100 m [8, 9]. According to a recent review paper [10], NLOS is currently the major problem for using GNSS in the applications of the intelligent transportation system in urbanised cities. As the majority of the NLOS receptions are caused by static buildings, various research studies [11–13] utilised 3D building models to identify the NLOS/line-of-sight (LOS) signals. Then, these NLOS receptions were

excluded from further GNSS positioning. Interestingly, recent research studies [14, 15] showed that dynamic vehicles can also cause GNSS NLOS and improvement was made by excluding NLOS receptions. However, excessive exclusion of NLOS measurements can significantly distort the satellite distribution as the majority of the GNSS measurements are NLOS in dense urban areas. As a result, GNSS positioning can be even worse after NLOS exclusion. An example is given in Fig. 1. The number of satellites will decrease dramatically if all the NLOS are excluded. More importantly, the value of the parameter, horizontal dilution of precision, which reflects the quality of satellite distribution increases significantly. Therefore, complete NLOS exclusion for dense urban areas is not preferable.

A well-known method, GNSS shadow matching, was studied to match the measured satellite visibility with the predicted satellite visibility of hypothesised positions [16–18]. However, the performance of shadow matching relies on the quality of satellite visibility classification and the initial guess of the GNSS receiver. A likelihood-based 3D-mapping-aided (3DMA) GNSS method, which modelled the measurement uncertainty to mitigate the NLOS and multipath effects, was also proposed to provide accurate positioning in the along-street direction [19]. Owing to the complementarity of shadow matching and likelihood-based 3DMA GNSS, their integration was recently studied [20] for better performance. Another range-based 3DMA GNSS method is to correct the NLOS affected measurement for GNSS positioning [21–24]. These methods were proposed to simulate signal transmission routes using the ray-tracing method [25].

However, the drawbacks of these ray-tracing-based 3DMA GNSS methods are the stringent requirements for (i) the accuracy of the 3D mapping database, (ii) the initial guess at receiver positions, and (iii) the computational power of the processors due to the ray-tracing process. Interestingly, the map of the environment can be constructed using 3D LiDAR and the map is used to classify the visibility of satellites. A research paper modelled the GNSS noise covariance through NLOS detection based on a LiDAR-constructed map [26]. Besides, incorporating the LiDAR map and 3D city model to exclude NLOS was conducted in the application of unmanned aerial vehicles [27].

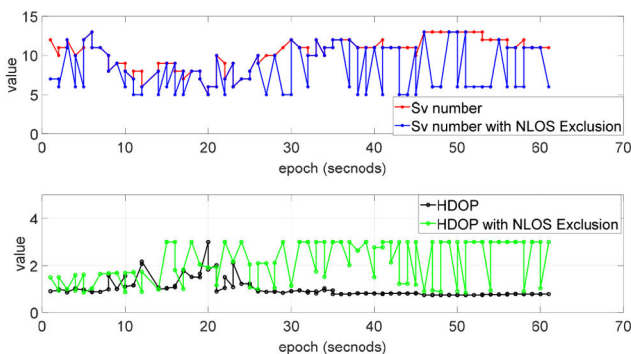


**Fig. 1** Illustration of the numbers of satellite measurements (GPS/BeiDou) before (red) and after (blue) NLOS exclusion in an urban canyon in Hong Kong

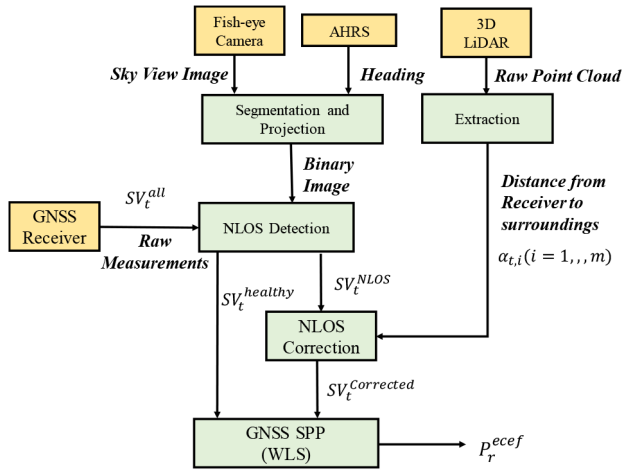


**Fig. 2** Overview of the proposed algorithm. The main inputs are GNSS raw measurements, the sky-view image from the fish-eye camera, and real-time 3D point clouds from the 3D LiDAR. The auxiliary input is the heading angle from the AHRS

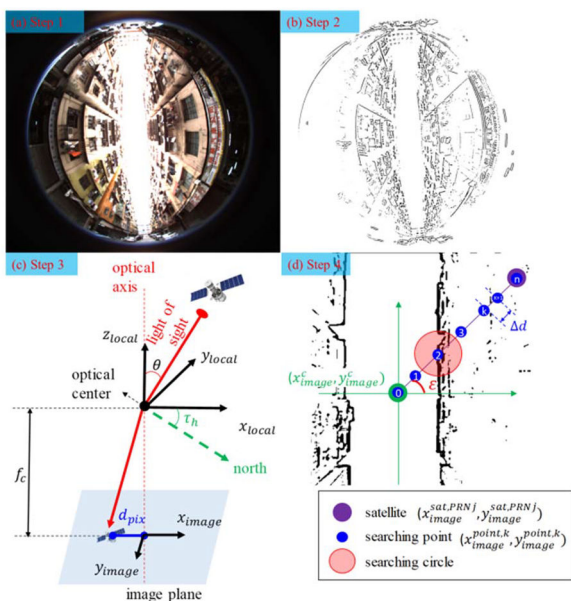


**Fig. 3** Illustration of the proposed method to classify satellite visibility by the image captured by a fish-eye camera. The four steps are (a) Step 1: coordination transformation from local frame to body frame, (b) Step 2: segmentation of sky and non-sky areas, (c) Step 3: projection of satellites in image coordinate, (d) Step 4: identification of satellite visibility

Recently, due to the fast development of the computer vision technique, the camera has been applied to capture the sky view to further identify the satellite visibility. To detect the visibility of satellites, the researchers apply omnidirectional and fish-eye cameras [28–30] to detect the sky views of the environment in the urbanised area. NLOS receptions can be detected with the detected sky views and improvements are made. Similar research studies [31, 32] are conducted recently and the improved GNSS positioning was integrated with visual simultaneous localisation and mapping [33]. However, these methods still tend to exclude NLOS receptions from GNSS positioning, which is not applicable in dense urban areas, such as Hong Kong, Tokyo, and New York. With the fast development of autonomous driving vehicles in the past few decades, the 3D light detection and ranging (LiDAR) system becomes an indispensable sensor that can provide abundant 3D point clouds. Compared with the optical scanning system, the 3D LiDAR sensor is more mature in terms of application in autonomous driving vehicles. In our team's previous work [34, 35], we employ the 3D LiDAR and building height to correct the NLOS receptions. Improved GNSS positioning was obtained with the NLOS correction method. However, the performance of this

method relies on the availability of a list of building height. Instead of relying on the building height, both a 3D LiDAR and a cost-effective sky-pointing monocular camera were employed to improve the GNSS positioning in our preliminary research in [36]. However, due to the limited field of view (FOV) of a monocular camera, satellite visibility cannot be fully classified.

Therefore, in this study, improving the GNSS single-point positioning (SPP) by detecting the GNSS NLOS receptions, and then correcting the NLOS receptions with the aid of real-time point clouds from a 3D LiDAR was proposed. A sky-pointing fish-eye camera was firstly applied to capture the sky-view image. Then, the sky and non-sky areas were segmented using an image-processing method. The GNSS satellites were projected into the segmented image with the aid of the heading angle of the camera provided by an attitude and heading reference system (AHRS). The satellite visibility could be identified based on the segmented image and the projected satellite positions inside the image. Instead of excluding the NLOS satellites, the NLOS pseudo-range measurements were corrected using a deterministic model of NLOS pseudo-range delay proposed in our previous work [8]. Finally, GNSS positioning was conducted using healthy measurements and corrected NLOS measurements.

The remainder of this paper is arranged as follows. An overview of the proposed method is presented in Section 2. The NLOS detection method by a sky-pointing fish-eye camera is presented in Section 3. The experiment evaluation is presented in Section 5 after the correction of GNSS NLOS with the 3D LiDAR is introduced in Section 4. Finally, the conclusions and future work are in Section 6.

## 2 Overview of the proposed method

In this study, detecting and correcting the NLOS receptions caused by surrounding objects, such as buildings, trees, and others, were proposed. To detect and correct the NLOS measurement, a method was proposed and its flowchart is shown in Fig. 2.

The GNSS raw measurements, including satellite elevation and azimuth angles and pseudo-range measurements, were obtained from the receiver. The sky-view image was collected using a sky-pointing fish-eye camera with a FOV of  $-90$  to  $+90^\circ$  vertically. The satellites were then projected into the segmented image with the aid of the heading angle from the AHRS. The LOS/NLOS measurements can be classified using the perceived and segmented sky-view image. The 3D LiDAR provided the point clouds of the surroundings. Therefore, the distance from the GNSS receiver to the surroundings can be obtained from the raw point clouds. The NLOS correction was then estimated using a deterministic NLOS model [8]. Finally, the GNSS SPP was conducted using a weighted least square (WLS).

## 3 GNSS NLOS detection using a fish-eye camera

The sky-view image captured from the fish-eye camera can effectively represent the geometry distribution of surrounding objects, such as buildings, tall dynamic vehicles, trees, and others. To determine the LOS/NLOS GNSS measurements using the sky-view image, four steps were proposed which can be seen in Fig. 3: (i) transform the raw sky-view image from the local frame [37] to the body (camera) frame [37] based on the heading angle from the AHRS; (ii) segment the sky-view image and separate the sky and non-sky areas; (iii) project the satellites onto the segmented image based on the satellite elevation and azimuth angles; (iv) identify the satellite visibility based on the segmented image and the satellite position inside the image.

*Step 1:* The raw image from the fish-eye camera was put in the body frame. In 3DMA GNSS [21], the 3D building models are usually projected onto the skyplot [38] together with the satellite to further determine whether the satellite is blocked by buildings. In this study, directly projecting the satellite onto the image to determine the satellite visibility was proposed. Therefore, the satellite in the local frame should be transformed into the same frame as an image in the body frame. Assuming that the fish-eye camera is a sky-pointing camera, only the globally referenced

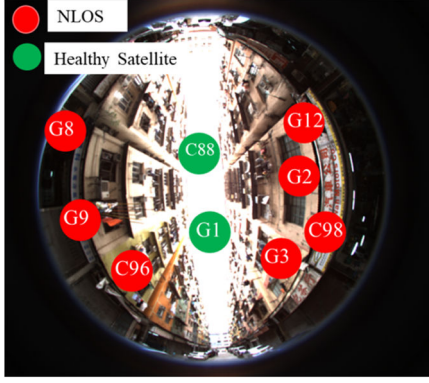


Fig. 4 Illustration of satellite visibility classification result

heading ( $\tau_h$ , see Fig. 3) of the vehicle (provided by AHRS) is required to transform the satellite into the body frame.

*Step 2:* To separate the sky and non-sky areas, we first transformed the colour image into a greyscale image. Then, the greyscale image was transformed into a binary image with an adaptive threshold. The noisy points inside the binary image were filtered by using a median filtering algorithm. These functions were performed using the OpenCV [39] library. The binary image is shown in Fig. 3b. If the satellite is located inside the sky area, the satellite is visible to the GNSS receiver and vice versa.

*Step 3:* To identify the satellite visibility based on the processed image in step 2, the satellite needs to be projected onto the same coordinate system. The illustration of projecting the satellite onto the image is shown in Fig. 3c which is a typical fish-eye projection model [40]. For each satellite associated with specific azimuth and elevation angles, it possesses a pixel position inside the sky-view image. We assumed that the optical centre of the camera is zenith pointing. To determine the position of the satellite inside the image, we needed, (i) the distance,  $d_{\text{pix}}$ , from the centre of the sky-view image in pixels which was correlated with the elevation angle,  $\varnothing_{\text{sat}}$ , of the satellite and (ii) the azimuth angle of the satellite. Assuming that the satellite was projected onto the image plane shown in Fig. 3c, the image coordinate system was inside the image plane.  $d_{\text{pix}}$  shown in Fig. 3c indicates the distance between the satellite position in the image and the centre of the image.  $d_{\text{pix}}$  is determined by the satellite elevation angle and the focal length ( $f_c$ ) of the fish-eye camera. Angle  $\theta$  satisfies

$$\theta = \frac{\pi}{2} - \varnothing_{\text{sat}} \quad (1)$$

Thus,  $d_{\text{pix}}$  can be expressed as follows [40]:

$$d_{\text{pix}} = 2 \cdot f_c \tan(\theta/2) \quad (2)$$

Given the centre of the sky-view image in a pixel position  $(x_{\text{image}}^c, y_{\text{image}}^c)$ , the position of the given satellite inside the sky-view image can be expressed as  $(x_{\text{image}}^{\text{sat}}, y_{\text{image}}^{\text{sat}})$

$$x_{\text{image}}^{\text{sat}} = x_{\text{image}}^c + d_{\text{pix}} \cos(\tau_h + \alpha_{\text{sat}}) \quad (3)$$

$$y_{\text{image}}^{\text{sat}} = y_{\text{image}}^c - d_{\text{pix}} \sin(\tau_h + \alpha_{\text{sat}}) \quad (4)$$

here  $\alpha_{\text{sat}}$  is the azimuth angle of the satellite.

*Step 4:* After the satellite is projected onto the sky-view image as shown in Fig. 3d, we proposed a searching method to identify the satellite visibility. For a given satellite (see Fig. 3d) located inside a sky-view image, identifying the visibility using Algorithm 1 was proposed.  $V_{\text{threshold}}$  represents the threshold of the mean pixel value and is experimentally determined. A satellite visibility classification result is shown in Fig. 4. The satellites were projected onto the image with the red and green dots denoting the NLOS and healthy measurements, respectively.

#### Algorithm 1: Satellite visibility identification

**Input:** binary image  $I_t$  shown in Fig. 3d, satellite position  $(x_{\text{image}}^{\text{sat}}, y_{\text{image}}^{\text{sat}})$  in pixels inside the image, and the radius of the searching circle:  $R_s$

**Output:** satellite visibility  $st_v$  (visible:  $st_v = 1$ , invisible:  $st_v = 0$ )

**S1:** initialise the searching point  $(x_{\text{image}}^{\text{point},0}, y_{\text{image}}^{\text{point},0}) = (x_{\text{image}}^c, y_{\text{image}}^c)$  starting from the centre of the image  $I_t$ ,  $st_v = 1$ , the searching direction represented by angle  $\epsilon$  (see Fig. 3d), which is calculated based on the satellite position in the image plane  $(x_{\text{image}}^{\text{sat}}, y_{\text{image}}^{\text{sat}})$

**S2:** given a constant incremental value  $\Delta d_{\text{pix}}$ , the searching point is updated as follows:

$$x_{\text{image}}^{\text{point},k} = x_{\text{image}}^{\text{point},k-1} + \Delta d_{\text{pix}} \cos(\epsilon) \quad (5)$$

$$y_{\text{image}}^{\text{point},k} = y_{\text{image}}^{\text{point},k-1} + \Delta d_{\text{pix}} \sin(\epsilon) \quad (6)$$

**S3:** given the searching point  $(x_{\text{image}}^{\text{point},k}, y_{\text{image}}^{\text{point},k})$  as the centre of the searching circle, calculate the mean value of pixel values of all the points inside the searching circle as follows:

$$\bar{V} = \sum_{i=1}^m I_t(x_{d,i}, y_{d,i}) \quad (7)$$

$I_t(x_{d,i}, y_{d,i})$  represents the pixel value of point  $i$  inside the searching circle with a radius of  $R_s$ .

**S4:** if  $\bar{V} > V_{\text{threshold}}$ , set  $st_v$  to 0.

**S5:** repeat steps 2 and 4 until the searching point reaches the position  $(x_{\text{image}}^{\text{sat}}, y_{\text{image}}^{\text{sat}})$  of the given satellite.

## 4 Improved GNSS positioning with NLOS correction

In this section, an NLOS error model is presented. NLOS error correction is implemented subsequently. Finally, GNSS positioning is conducted by WLS.

### 4.1 NLOS correction based on LiDAR point clouds

In terms of the measurements from the GNSS receiver, each pseudo-range measurement  $\rho_n$  is written as follows [41]:

$$\rho_n = R_n + c(\delta t^r - \delta t_n^{\text{sv}}) + I_n + T_n + e_n \quad (8)$$

where  $R_n$  is the geometric range between the satellite and the GNSS receiver,  $\delta t_n^{\text{sv}}$  denotes the satellite clock bias, and  $\delta t^r$  indicates the receiver clock bias.  $I_n$  represents the ionospheric delay distance;  $T_n$  indicates the tropospheric delay distance.  $e_n$  represents the errors caused by the multipath effects, NLOS receptions, receiver noise, antenna delay, and others. In this study, we focused on mitigating the NLOS errors caused by the related environment buildings. In other words, shrinking  $e_n$  by mitigating NLOS errors. The NLOS error model was proposed in [8].  $\alpha$  represents the distance from the receiver to the building. It was assumed that the building was vertical to the ground and GNSS signal reflection satisfied the law of reflection. The direction of actual signal transmission was parallel to the direction of the expected signal transmission. Route distance difference  $\gamma$  between the reflected signal and the expected signal is expressed as follows [8]:

$$\gamma = \alpha \sec \varnothing_{\text{sat}} (1 + \cos 2\varnothing_{\text{sat}}) \quad (9)$$

Thus, the NLOS error can be calculated with the elevation angle and the distance from the receiver to the building causing the reflection. In this study, the distance from the GNSS receiver was directly provided by the 3D LiDAR point clouds. The details about



Fig. 5 Experimental vehicle and sensor setup in the left figure. Test scenarios of urban canyons 1 and 2

Table 1 Parameter values used in this paper

Parameters	$V_{\text{threshold}}$	$\Delta d_{\text{pix}}$	FOV	$f_c$
value	50	5 pixels	(H/V) 185°	583 pixels

Table 2 Performance of the GNSS SPP in urban Canyon 1

GNSS Positioning	WLS	WLS-NE	WLS-NC
mean error	27.18 m	58.57 m	18.49 m
std	22.28 m	86.13 m	15.27 m
maximum error	131.81 m	156.29 m	73.37 m
availability	100%	9.70%	100%

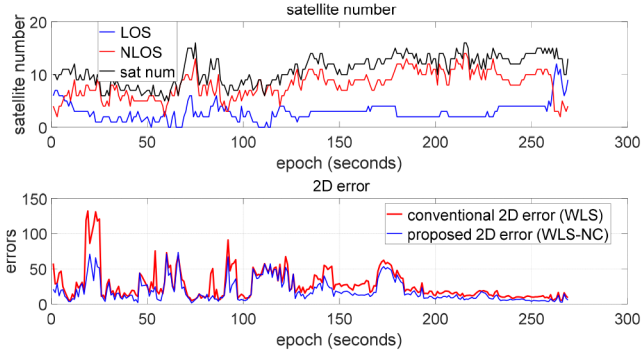


Fig. 6 2D positioning error of the listed GNSS positioning methods in urban canyon 1

NLOS correction implementation can be found in the previous work of our team in [34].

#### 4.2 GNSS positioning based on corrected pseudo-range measurements

The clock bias between the GNSS receiver and the satellites is usually represented by the pseudo-range measurements. The equation linking the receiver and the satellite positions can be expressed as the following linearised formula using the least square (LS) method:

$$\hat{\mathbf{x}} = (\mathbf{G}^T \mathbf{G})^{-1} \mathbf{G}^T \boldsymbol{\rho} \quad (10)$$

where  $\mathbf{G}$  represents the observation matrix and consists of unit LOS vectors between GNSS receivers' position and the satellite position.  $\hat{\mathbf{x}}$  indicates the estimated receiver position and  $\boldsymbol{\rho}$  denotes the pseudo-range measurements vector. Note that both the healthy and corrected pseudo-range measurements were used. Conventionally, to better represent the reliability of each measurement based on the information measured by the receiver, weightings of each measurement are needed. The function to calculate the weighting by integrating the measurement  $C/N_0$  and the satellite elevation angle is expressed as  $W$  [42]. Finally, the GNSS receiver position can be estimated using the WLS method as

$$\hat{\mathbf{x}} = (\mathbf{G}^T \mathbf{W} \mathbf{G})^{-1} \mathbf{G}^T \mathbf{W} \boldsymbol{\rho} \quad (11)$$

where pseudo-range vector  $\boldsymbol{\rho}$  includes both the LOS and corrected NLOS measurements. In this case, both the LOS and NLOS measurements were applied to the GNSS positioning calculation.

## 5 Experiment evaluation

### 5.1 Experiment setup

To validate the effectiveness of the proposed method, two experiments were conducted in typical urban canyons of Hong Kong on 12 July 2019. The experimental scenes are shown in Fig. 5. The left figure of Fig. 5 shows the test vehicle with all the sensors installed in a compact sensor kit. The middle and right figures show the tested urban canyons 1 and 2. The tested urban scenarios contain static buildings, trees, and dynamic objects.

In both experiments, a u-blox M8 T GNSS receiver was used to collect raw global positioning system (GPS)/BeiDou measurements at the frequency of 1 Hz. The sky-pointing fish-eye camera was employed to capture the sky-view image at the frequency of 10 Hz. The Xsens Ti-10 IMU (which can also act as an AHRS) was employed to collect data at the frequency of 100 Hz to provide the heading angle for the fish-eye camera. In addition, the NovAtel SPAN-CPT, a GNSS real-time kinetic/INS (fibre optic gyroscopes) integrated navigation system, was used to provide the ground truth. All the data were collected and synchronised under the robot operation system [43]. The coordinate systems between all the sensors were calibrated before the experiments. The values of the applied parameters in this study are shown in Table 1.

To verify the effectiveness of the proposed method, three GNSS positioning methods were compared:

- WLS [44]
- WLS + NLOS exclusion (WLS-NE) — excluding the NLOS measurements detected using a fish-eye camera and performing WLS.
- WLS + NLOS correction (WLS-NC) — correcting the NLOS measurements detected using a fish-eye camera and performing WLS.

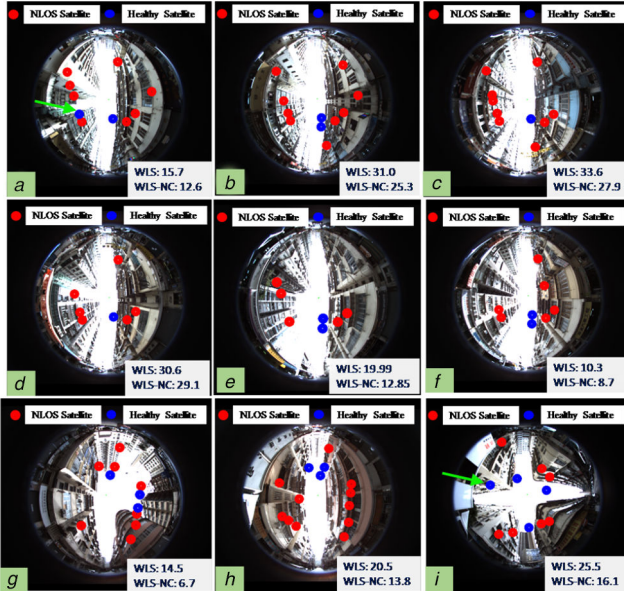
### 5.2 Evaluation in urban canyon 1 experiment

In urban canyon 1, both sides of the road are regular buildings of almost similar heights which is suitable for NLOS detection and correction. We first experimented in urban canyon 1 to validate the performance of the proposed method. The GNSS positioning performance of the listed three methods is shown in Table 2. A mean positioning error of 27.18 m was obtained using the conventional WLS method, with the maximum error reaching 131.81 m. After all the NLOS satellites detected using the fish-eye camera being excluded from WLS calculation, the positioning error increased to >58 m. Moreover, the standard deviation also increased from 22.28 to 86.13 m. As a result of the excessive NLOS exclusion, the availability of GNSS positioning decreased from 100 to 9.70%. With the help of the proposed NLOS detection and correction method, the GNSS positioning error decreased to 18.49 m and the standard deviation also decreased slightly compared with that of the WLS. The improved GNSS positioning performance showed the effectiveness of the proposed method. Moreover, the availability of the proposed method was also guaranteed using the proposed method. The detailed positioning errors of the WLS and WLS-NC are shown in Fig. 6. The upper graph shows the number of LOS and NLOS satellites. The lower graph shows the positioning error using the WLS and proposed method. It can be seen that the proposed method outperforms the WLS almost throughout the test.

The LOS/NLOS satellite numbers are shown in Table 3. The mean numbers of LOS and NLOS satellites are 2.89 and 8.08, respectively. During the experiments, the NLOS satellites made up 73.65% of all the satellites due to the blockage from the surrounding tall buildings. The minimum number of LOS satellites was 0, which means all the satellites were NLOS receptions during this epoch. Interestingly, at least 2 satellites were NLOS during the experiment and the maximum number of NLOS satellites reached 14.

**Table 3** Satellite numbers in urban canyon 1

Satellite	LOS	NLOS	LOS & NLOS
mean number	2.89	8.08	10.97
std	1.75	2.54	2.49
max number	12	14	16
min number	0	2	5
percentage	26.34%	73.65%	—

**Fig. 7** Illustration of sky-plot which indicates the satellite distribution during the dynamic experiment. Green dots represent healthy satellites. Red dots denote the NLOS satellites

(a) Epoch with 8 NLOS and 2 LOS satellites, (b) Epoch with 9 NLOS and 2 LOS satellites, (c) Epoch with 9 NLOS and 1 LOS satellites, (d) Epoch with 6 NLOS and 1 LOS satellites, (e) Epoch with 5 NLOS and 2 LOS satellites, (f) Epoch with 6 NLOS and 2 LOS satellites, (g) Epoch with 8 NLOS and 3 LOS satellites, (h) Epoch with 11 NLOS and 3 LOS satellites, (i) Epoch with 7 NLOS and 4 LOS satellites

**Table 4** LOS/NLOS detection accuracy based on two heading angle sources

Heading source	LOS	NLOS
AHRS (Xsens Ti-10 IMU)	93.01%	89.61%
reference system (NovAtel SPANCPT)	96.33%	95.20%

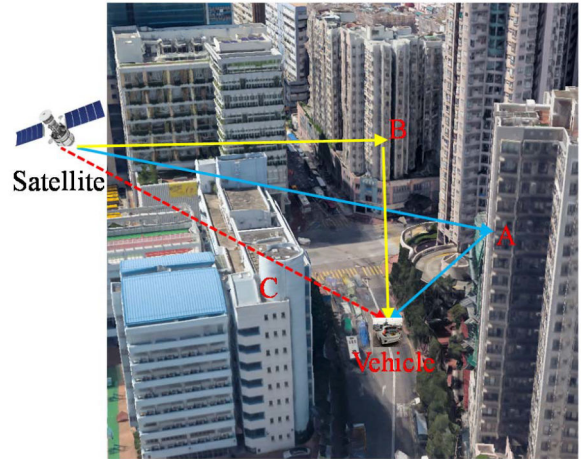
**Table 5** NLOS pseudo-range correction (epoch 459017)

Satellite Pseudorandom noise (PRN)	Elevation angle	$C/N_0$ , dB-Hz	Actual pseudo-range correction	Estimated pseudo-range correction
5	41.18°	30	1.54 m	6.41 m
17	52.47°	24	3.33 m	2.45 m
19	63.65°	26	0 m	0.93 m
88	48.13°	27	14.14 m	9.86 m
99	45.12°	24	5.17 m	10.07 m
113	52.14°	25	5.2 m	3.45 m
116	46.83°	36	12.51 m	11.52 m

The satellite distributions inside the sky-view image in several epochs are shown in Fig. 7. The red circle shows the NLOS satellite and blue circle shows the healthy satellite. The numbers inside the figures show the accuracy of WLS and WLS-NC, respectively. As the satellite classification accuracy relies on the performance of the image processing presented in Section 3, some of the NLOS satellites can be misclassified due to the illumination sensitivity of the image-processing algorithm. For example, the

**Table 6** NLOS pseudo-range correction (epoch 459069)

Satellite PRN	Elevation angle	$C/N_0$ , dB-Hz	Actual pseudo-range correction	Estimated pseudo-range correction
2	38.27°	30	14.91 m	9.73 m
5	41.50°	28	9.42 m	6.33 m
6	44.96°	26	11.95 m	12.28 m
9	30.73°	25	10.18 m	6.49 m
12	29.64°	33	61.01 m	7.98 m
17	52.24°	41	11.37 m	5.89 m
89	64.57°	32	7.98 m	10.37 m
94	47.65°	25	7.52 m	11.07 m

**Fig. 8** Illustration NLOS signal transmission which can be reflected by reflector A or B

satellites near the building boundaries are misclassified, as shown in Figs. 7a and i.

In short, the improved GNSS positioning accuracy in Table 2 and Fig. 6 shows the effectiveness of the proposed method. NLOS detection performance is shown in Table 3 and Fig. 7. To find out the correctness of the applied NLOS correction estimation method presented in Section 4, we compared the estimated pseudo-range delay (9) of the NLOS satellites using the proposed method with the exact pseudo-range delay acquired by using the ray-tracing method [21] (Table 4). Our previous work [21] employed the building model and ray-tracing technique to recover the exact NLOS delay caused by the reflection from the surrounding buildings. Based on the ground truth position of the GNSS receiver provided by the reference system, the potential NLOS pseudo-range delay can be accurately recovered. Tables 5 and 6 show the estimated and ground truth delays in several NLOS measurements in two epochs.

In Table 5, all seven satellites have an elevation angle of  $>40^\circ$ . In general, a satellite with a low elevation angle is more likely to cause a larger NLOS delay [8]. According to (9), the NLOS delay in the pseudo-range domain is determined by the satellite elevation angle and the distance from the GNSS receiver to the signal reflector. Therefore, satellite 88 with a larger elevation angle (48.13°) can even cause a larger NLOS delay (14.14 m) than satellite 5 (1.54 m). Besides, satellite 113 with small  $C/N_0$  (25 dB-Hz) conversely has a smaller correction, compared with the one caused by satellite 116 (36 dB-Hz). It can be seen from Table 5 that some of the estimated NLOS delays are close to the actual NLOS delay, e.g. satellites 17, 88, 113, and 116. One of the reasons that the proposed method cannot perfectly estimate the actual NLOS delay is that the proposed method relies on the detection of the NLOS signal reflector. The reflector can be misidentified using the proposed method, as illustrated in Fig. 8. The GNSS signal transmitted can be reflected by building A or B. In fact, the distance from the GNSS receiver to building B was significantly larger than that of building A, causing a larger NLOS delay. Therefore, if the NLOS signal reflector is not correctly detected,

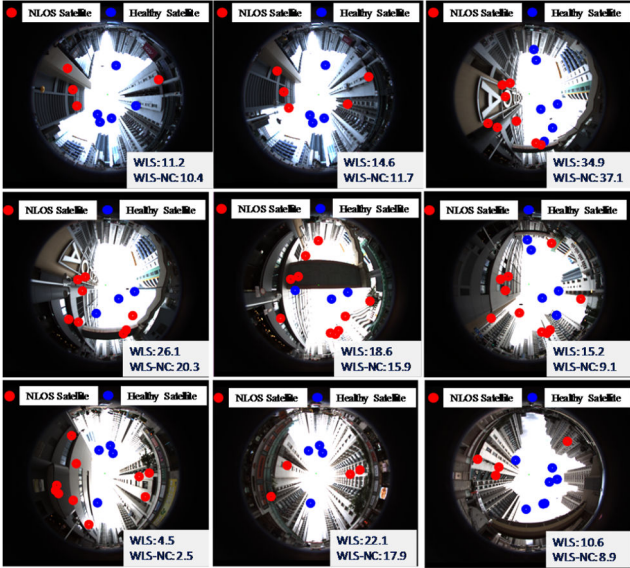


Fig. 9 Illustration of sky-plot indicating satellite distribution during the dynamic experiment. Green dots represent healthy satellites. Red dots represent the NLOS satellites

Table 7 Positioning performance of the GNSS SPP in urban canyon 2

GNSS positioning	WLS	WLS-NE	WLS-NC
mean error	17.51 m	35.19 m	12.07 m
std	8.97 m	22.07 m	7.09 m
maximum error	55.80 m	85.01 m	43.45 m
availability	100%	35.88%	100%

the estimated NLOS correction cannot introduce enough improvement. To demonstrate this issue, another NLOS correction result is shown in Table 6. In this epoch, the actual NLOS delay for satellite 12 was 61.01 m and the estimated one was only 7.98 m. The NLOS satellite with a low elevation angle is more likely to be reflected by buildings far away. However, the proposed method can still help to correct the NLOS delay even in this case, although the improvement was not remarkable. In short, the proposed method can improve the GNSS positioning from 27.18 to 18.49 m in the test in urban canyon 1.

### 5.3 Evaluation in urban canyon 2 experiment

To verify the performance of the proposed method in this study, we conducted another experiment in urban canyon 2 with irregular building distribution where the heights of the buildings on both sides were diverse (see Fig. 5 and for the sky-view image, see Fig. 9). In such a case, the NLOS signal reflector detection can be significantly harder than in urban canyon 1. Therefore, we believe that urban canyon 2 is harder to obtain improvement compared with the test in urban canyon 1.

The GNSS positioning results using the listed three methods are shown in Table 7. A mean positioning error of 17.51 m was obtained using the conventional WLS method and positioning solution availability of 100% was obtained. The mean error increased to 35.19 m with all the NLOS measurements excluded. Moreover, the maximum error also slightly increased from 55.80 to 85.01 m. The availability decreased to 35.88% due to the excessive NLOS exclusion. With the aid of the proposed method, the mean error decreased to 12.07 m and the standard deviation also decreased to 7.09 m. The availability was also guaranteed. Fig. 10 shows the details about the 2D positioning error during the test in urban canyon 2. The upper graph shows the satellite number. The lower graph shows GNSS positioning error using the WLS and WLS-NC methods.

The mean number of LOS satellites was 5.03 which was larger than that in urban canyon 1 (shown in Table 8). The percentages of

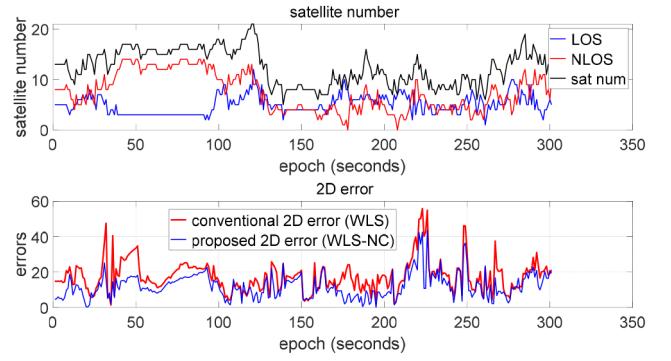


Fig. 10 2D positioning error of the listed GNSS positioning methods in urban canyon 2

Table 8 Satellite numbers in urban canyon 2

Satellite	LOS	NLOS	LOS & NLOS
mean number	5.03	7.42	12.45
std	1.86	3.74	3.48
max number	12	14	21
min number	1	0	5
percentage	40.40%	59.60%	—

LOS and NLOS satellites were 40.40 and 59.60%, respectively. The sky-view images in some epochs are shown in Fig. 9. It can be seen that the building boundary distribution was not as regular as that in urban canyon 1 (see Fig. 7). Therefore, the detection of the NLOS signal reflector was more difficult to be identified as the reflector could be a building far away from the ego-vehicle (see Fig. 8). However, improved GNSS positioning accuracy was still achieved, with the mean error decreasing from 17.51 to 12.07 m, which again shows the effectiveness of the proposed method.

## 6 Conclusions and future work

Insufficient positioning accuracy and robustness is one of the main problems preventing the arrival of autonomous vehicles. As mentioned in [10], NLOS is the major cause of unsatisfactory GNSS positioning results in super-urbanised cities. NLOS exclusion is a commonly studied method to improve GNSS positioning and improvements can be obtained in sub-urban scenarios.

To correct the NLOS pseudo-range errors without relying on the time-consuming ray-tracing process, in this study, detecting the NLOS receptions and correcting the NLOS measurements with the aid of real-time point clouds and a fish-eye camera was proposed. The fish-eye camera is firstly applied to capture the sky-view image. Then the sky-view image was segmented, and the satellites were projected into the segmented image. The NLOS satellites were detected accordingly. Instead of excluding the NLOS receptions from GNSS positioning calculation, the NLOS measurements were corrected by using an NLOS model. Both the healthy and corrected pseudo-range measurements were employed to conduct the GNSS positioning. The accuracy was improved both in urban canyons 1 and 2, which shows the effectiveness of the proposed method.

In the near future, the NLOS signal reflector detection method will be studied. To improve the sky-view image segmentation accuracy, we will adopt the deep learning-based image segmentation method to enhance the satellite classification method. Moreover, we will study the integration of GNSS and INS [3] by using the proposed NLOS correction method to find out the potential of the proposed method in GNSS/INS fusion for autonomous systems [2].

## 7 References

- [1] Wen, W., Zhou, Y., Zhang, G., *et al.*: 'Urbanloco: a full sensor suite dataset for mapping and localization in urban scenes', 2019
- [2] Sergiyenko, O.Y., Ivanov, M.V., Tyrsa, V., *et al.*: 'Data transferring model determination in robotic group', *Robot. Auton. Syst.*, 2016, **83**, pp. 251–260
- [3] Castro-Toscano, M.J., Rodríguez-Quíñonez, J.C., Hernández-Balbuena, D., *et al.*: 'A methodological use of inertial navigation systems for strapdown navigation task'. 2017 IEEE 26th Int. Symp. on Industrial Electronics (ISIE), Edinburgh, UK, 2017
- [4] Levinson, J., Thrun, S.: 'Robust vehicle localization in urban environments using probabilistic maps'. 2010 IEEE Int. Conf. on Robotics and Automation (ICRA), Anchorage, AK, USA, 2010, pp. 4372–4378
- [5] Fernandez, A., Wis, M., Dovis, F., *et al.*: 'GNSS/INS/LiDAR integration in urban environment: algorithm description and results from Atenea test campaign'. 2012 6th ESA Workshop on Satellite Navigation Technologies and European Workshop on GNSS Signals and Signal Processing, (NAVITEC), Noordwijk, Netherlands, 2012
- [6] Wen, W., Zhang, G., Hsu, L.-T.: 'Object detection aided GNSS and its integration with LiDAR in highly urbanized areas', *IEEE Intell. Transp. Syst. Mag.*, 2019, accepted
- [7] Wen, W., Bai, X., Kan, Y.-C., *et al.*: 'Tightly coupled GNSS/INS integration via factor graph and aided by fish-eye camera', *IEEE Trans. Veh. Technol.*, 2019, **68**, (11), pp. 10651–10662
- [8] Hsu, L.-T.: 'Analysis and modeling GPS NLOS effect in highly urbanized area', *GPS Solut.*, 2018, **22**, (1), p. 7
- [9] Kong, S.H.: 'Statistical analysis of urban GPS multipaths and pseudo-range measurement errors', *IEEE Trans. Aerosp. Electron. Syst.*, 2011, **47**, (2), pp. 1101–1113
- [10] Breßler, J., Reisdorf, P., Obst, M., *et al.*: 'GNSS positioning in non-line-of-sight context—a survey'. 2016 IEEE 19th Int. Conf. on Intelligent Transportation Systems (ITSC), Rio de Janeiro, Brazil, 2016
- [11] François, P., David, B., Florian, M.: 'Non-line-of-sight GNSS signal detection using an on-board 3D model of buildings'. 2011 11th Int. Conf. on ITS Telecommunications (ITST), St. Petersburg, Russia, 2011
- [12] Groves, P.D., Jiang, Z., Wang, L., *et al.*: 'Intelligent urban positioning using multi-constellation GNSS with 3D mapping and NLOS signal detection'. Proc. 25th Int. Tech. Meet. Satell. Div. Inst. Navig. (ION GNSS 2012), Nashville, TN, USA, September 2012, pp. 458–472
- [13] Peyraud, S., Bétaille, D., Renault, S., *et al.*: 'About non-line-of-sight satellite detection and exclusion in a 3D map-aided localization algorithm', *Sensors*, 2013, **13**, (1), pp. 829–847
- [14] Wen, W., Zhang, G., Hsu, L.-T.: 'Exclusion of GNSS NLOS receptions caused by dynamic objects in heavy traffic urban scenarios using real-time 3d point cloud: an approach without 3D maps'. 2018 IEEE/ION Position, Location and Navigation Symposium (PLANS), 2018
- [15] Wen, W., Zhang, G., Hsu, L.-T.: 'GNSS NLOS exclusion based on dynamic object detection using LiDAR point cloud', *IEEE Trans. Intell. Transp. Syst.*, 2019
- [16] Wang, L., Groves, P.D., Ziebart, M.K.: 'Urban positioning on a smartphone: real-time shadow matching using GNSS and 3d city models', The Institute of Navigation, 2013
- [17] Wang, L., Groves, P.D., Ziebart, M.K.: 'GNSS shadow matching: improving urban positioning accuracy using a 3D city model with optimized visibility scoring scheme', *Navigation*, 2013, **60**, (3), pp. 195–207
- [18] Wang, L., Groves, P.D., Ziebart, M.K.: 'Smartphone shadow matching for better cross-street GNSS positioning in urban environments', *J. Navig.*, 2015, **68**, (3), pp. 411–433
- [19] Groves, P.D., Adjrad, M.: 'Likelihood-based GNSS positioning using LOS/NLOS predictions from 3D mapping and pseudoranges', *GPS Solut.*, 2017, **21**, (4), pp. 1805–1816
- [20] Adjrad, M., Groves, P.D.: 'Intelligent urban positioning: integration of shadow matching with 3D-mapping-aided GNSS ranging', *J. Navig.*, 2018, **71**, (1), pp. 1–20
- [21] Hsu, L.-T., Gu, Y., Kamijo, S.: '3D building model-based pedestrian positioning method using GPS/GLONASS/QZSS and its reliability calculation', *GPS Solut.*, 2016, **20**, (3), pp. 413–428
- [22] Miura, S., Hsu, L.-T., Chen, F., *et al.*: 'GPS error correction with pseudorange evaluation using three-dimensional maps', *IEEE Trans. Intell. Transp. Syst.*, 2015, **16**, (6), pp. 3104–3115
- [23] Obst, M., Bauer, S., Reisdorf, P., *et al.*: 'Multipath detection with 3D digital maps for robust multi-constellation GNSS/INS vehicle localization in urban areas'. Intelligent Vehicles Symp. (IV), 2012 IEEE, Alcalá de Henares, Spain 2012
- [24] Suzuki, T., Kubo, N.: 'Correcting GNSS multipath errors using a 3d surface model and particle filter'. Proc. ION GNSS+2013, Nashville, TN, USA, 2013
- [25] Lee, Y.-W., Suh, Y.-C., Shibasaki, R.: 'A simulation system for GNSS multipath mitigation using spatial statistical methods', *Comput. Geosci.*, 2008, **34**, (11), pp. 1597–1609
- [26] Maier, D., Kleiner, A.: 'Improved GPS sensor model for Mobile robots in urban terrain'. 2010 IEEE Int. Conf. on Robotics and Automation (ICRA), 2010
- [27] Shetty, A., Gao, G.X.: 'Covariance estimation for GPS-LiDAR sensor fusion for UAVs'. ON GNSS+2017, Portland, OR, USA, 2017
- [28] Meguro, J.I., Murata, T., Takiguchi, J.I., *et al.*: 'GPS multipath mitigation for urban area using omnidirectional infrared camera', *IEEE Trans. Intell. Transp. Syst.*, 2009, **10**, (1), pp. 22–30
- [29] Suzuki, T., Kitamura, M., Amano, Y., *et al.*: 'High-accuracy GPS and GLONASS positioning by multipath mitigation using omnidirectional infrared camera'. IEEE Int. Conf. on Robotics and Automation, Shanghai, People's Republic of China, 2011
- [30] Sánchez, J.S., Gerhmann, A., Thevenon, P., *et al.*: 'Use of a fish-eye camera for GNSS NLOS exclusion and characterization in urban environments'. ION ITM 2016, International Technical Meeting, ION, 2016
- [31] Gakne, P.V.: 'Improving the accuracy of GNSS receivers in urban canyons using an upward-facing camera', PhD thesis, Geomatics Engineering, University of Calgary, 2018
- [32] Gakne, P.V., O'Keefe, K.: 'Tightly-coupled gnss/vision using a sky-pointing camera for vehicle navigation in urban areas', *Sensors*, 2018, **18**, (4), p. 1244
- [33] Mur-Artal, R., Montiel, J.M.M., Tardos, J.D.: 'Orb-slam: a versatile and accurate monocular slam system', *IEEE Trans. Robot.*, 2015, **31**, (5), pp. 1147–1163
- [34] Wen, W., Zhang, G., Hsu, L.-T.: 'Correcting GNSS NLOS by 3D LiDAR and building height'. ION GNSS+, 2018, Miami, FL, USA, 2018
- [35] Wen, W., Zhang, G., Hsu, L.-T.: 'Correcting NLOS by 3D LiDAR and building height to improve GNSS single point positioning', *Navigation*, 2019, **66**, (4), pp. 705–718
- [36] Bai, X., Wen, W., Zhang, G., *et al.*: 'Real-time GNSS NLOS detection and correction aided by sky-pointing camera and 3D LiDAR'. Proc. ION Pacific PNT 2019, Honolulu, HI, USA, 2019
- [37] Groves, P.D.: 'Principles of GNSS, inertial, and multisensor integrated navigation systems' (Artech house, London, UK, 2013)
- [38] Marshall, J.: 'Creating and viewing skyplots', *GPS Solut.*, 2002, **6**, (1–2), pp. 118–120
- [39] Bradski, G., Kaehler, A.: 'Opencv', *Dr. Dobb's J. Softw. Tools*, 2000, **3**, pp. 1–81
- [40] Kannala, J., Brandt, S.S.: 'A generic camera model and calibration method for conventional, wide-angle, and fish-eye lenses', *IEEE Trans. Pattern Anal. Mach. Intell.*, 2006, **28**, (8), pp. 1335–1340
- [41] Kaplan, E., Hegarty, C.: 'Understanding GPS: principles and applications' (Artech house, London, UK, 2005)
- [42] Realini, E., Reguzzoni, M.: 'goGPS: open source software for enhancing the accuracy of low-cost receivers by single-frequency relative kinematic positioning', *Meas. Sci. Technol.*, 2013, **24**, (11), p. 115010
- [43] Quigley, M., Conley, K., Gerkey, B., *et al.*: 'ROS: an open-source robot operating system'. ICRA Workshop on Open Source Software, Kobe, Japan, 2009
- [44] Herrera, A.M., Suhandri, H.F., Realini, E., *et al.*: 'goGPS: open-source Matlab software', *GPS Solut.*, 2016, **20**, (3), pp. 595–603